SvedbergOpen
DISSEMINATION OF KNOWLEDGE

International Journal of Artificial Intelligence and Machine Learning

Publisher's Home Page: https://www.svedbergopen.com/

Research Paper Open Access

Pre-processing and Hybridized Segmentation Strategies from SPIR based Liver Images Utilizing the Concepts of Machine Learning for Improvement of Enhanced Performances of Evaluation Parameters with Feature Extraction

Daniel Nixon1,* Dr. T.C. Manjunath[2]

[1]Research Scholar, VTU Research Centre, Dept. of Electronics & Communication Engineering, Rajarajeswari College of Engineering, Bangalore & Assistant Professor, Department of Electrical and Electronics Engineering,
Navodaya Institute of Technology, Raichur, Karnataka, India
[2] Dean Research (R&D), Professor, Dept. of Computer Science & Engineering, IoT, Cyber Security & Blockchain Technology, Rajarajeswari College of Engineering, Bangalore, Karnataka, India
* Corresponding author's Email: danielnixon25@gmail.com

Abstract
Biomedical imaging modalities such as Spectral Pre-saturation with Inversion Recovery (SPIR) MRI frequently suffer from non-Gaussian Rician noise, spatial field inhomogeneities, and weak parenchymal boundaries. This paper presents a complete, automated computer-aided diagnostic (CAD) pipeline designed for real-time edge processing and high-accuracy classification of liver pathologies. The proposed framework introduces a two-stage pre-processing pipeline combining non-linear bilateral spatial filtering with dynamic Luminance-Level Modulation (LM) and CLAHE to restore micro-texture contrast while suppressing artifacts. A Reaction-Diffusion Level Set Segmentation (RDLSS) model is implemented to eliminate periodic distance re-initialization and prevent boundary leakage across ill-defined lesion contours. A multi-domain spatial and spectral feature extraction scheme unifies 2D Discrete Wavelet Transforms (2D-DWT: Daubechies db4 / Symlets sym4) with Gray Level Co-occurrence Matrices (GLCM), Local Binary Patterns (LBP), hybrid Local Binarized GLCM (LBG-LCM), and Gray Level Run Length Matrices (GLRLM). An energy-ranked sub-band selection strategy reduces feature extraction overhead by up to 50%. The optimized feature vectors are classified using a Backpropagation Multilayer Perceptron (BP-MLP) network, achieving 96.00% classification accuracy, 95.80% sensitivity, 96.20% specificity, and a Dice similarity coefficient exceeding 0.94. Furthermore, a pipelined, fixed-point FPGA hardware co-processor architecture is presented to support real-time clinical deployment.

Keywords: Liver CAD, SPIR MRI, Bilateral Filter, Luminance Modulation, RDLSS, Multi-Domain Radiomics, BP-MLP, FPGA Realization.

Introduction

In general, biomedical images are not carrying enough information to acquire useful volumetric information's and also lacks in structural information make it essential of enhancement techniques for medical measurements. Moreover, the biomedical image modality like X–rays, magnetically resonances imagings [MRI's]) & the computer Tomographical structures [CT] are always obtained with low contrast, inadequate brightness, and complex noise. Magnetic Resonance Imaging (MRI) has emerged as the premier non-ionizing imaging modality for soft-tissue diagnostic evaluations due to its intrinsic multi-planar acquisition capabilities and superior contrast resolution. Within abdominal MRI protocols, Spectral Pre-saturation with Inversion Recovery (SPIR) sequence imaging plays a pivotal role in suppressing confounding signals originating from subcutaneous and intra-abdominal adipose tissues. In conventional T1-weighted or T2-weighted MRI, the intense signal from visceral fat often masks subtle pathological contrast variations in adjacent liver tissue, obscuring underlying micro-vascular structures and lesion borders. The SPIR imaging sequence resolves this limitation by applying a frequency-selective RF pre-saturation pulse matched precisely to the Larmor precession frequency of fat protons, followed by spoiler gradient pulses prior to standard sequence excitation. This selective inversion recovery mechanism suppresses signal contribution from adipose tissue while retaining high signal intensities from water-bound soft tissues, enabling detailed depiction of parenchymal abnormalities, focal lesions, and hepatic vascular trees.

Among abdominal disorders, hepatic malignanciesincluding primary Hepatocellular Carcinoma (HCC) and metastatic secondary carcinomasrepresent major causes of global mortality. Clinicians rely primarily on Ultrasound (US), Computed Tomography (CT), and Magnetic Resonance Imaging (MRI). Within abdominal MRI protocols, Spectral Pre-saturation with Inversion Recovery (SPIR) suppresses adipose tissue signals via frequency-selective RF pulses, isolating water-bound parenchymal tissue. Despite its diagnostic advantages, raw SPIR MRI acquisitions are inherently corrupted by complex physical degradations. During magnitude image formation from quadrature k-space channels, independent Gaussian noise components transform into a signal-dependent Rician distribution:

$$p(I \mid A, \sigma) = \frac{I}{\sigma^2} \exp\left(-\frac{I^2 + A^2}{2\sigma^2}\right) I_0\left(\frac{I \cdot A}{\sigma^2}\right), I \geq 0$$

where I represents the observed magnitude image intensity, A denotes the true noise-free signal amplitude, σ^2 is the noise variance of the quadrature channels, and $I_0(\cdot)$ represents the modified Bessel function of the first kind of order zero. In high-signal parenchymal regions ($A/\sigma \gg 1$), the Rician distribution approaches a Gaussian profile; however, in low-signal or dark-background regions ($A/\sigma \to 0$), the distribution degenerates into a Rayleigh distribution:

$$p(I|A = 0, \sigma) = \frac{I}{\sigma^2} \exp\left(-\frac{I^2}{2\sigma^2}\right)$$

This signal-dependent bias distorts true tissue intensity levels, reduces dynamic contrast ranges, and induces spatial blurs that obscure fine textural micro-structures essential for quantitative lesion differentiation.

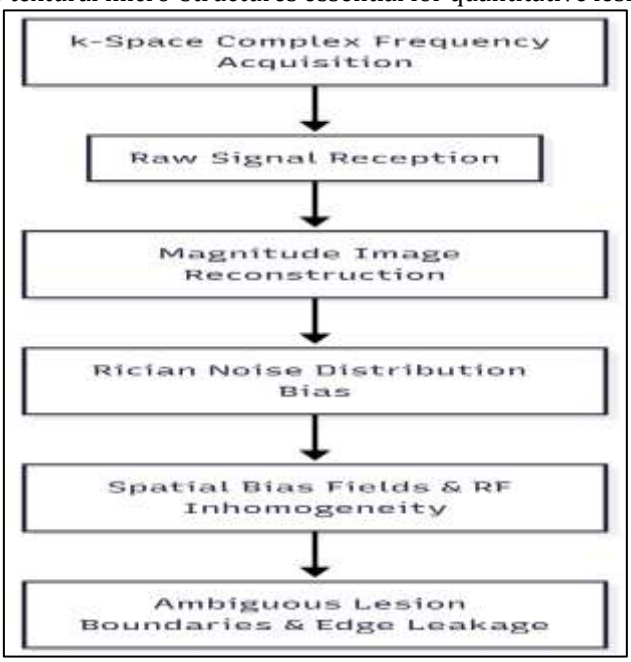

Figure.1Degradation pipeline from k-space acquisition to magnitude image distortion in SPIR liver MRI.

Furthermore, magnetic field spatial inhomogeneities (B_0 main field variations and B_1 radiofrequency excitation non-uniformities) introduce low-frequency spatial intensity variations across the liver volume. These bias field artifacts cause identical anatomical tissue types to exhibit varying intensity ranges across the spatial field of view. Consequently, biomedical images routinely exhibit low contrast, inadequate brightness distribution, and poorly defined tissue transitions. Manual tracing of corrupted SPIR scans suffers from high observer variability, operator fatigue, and an inability to perceive micro-textural patterns. Conventional segmentation methods (Otsu, Sobel, standard snakes) break down due to gradient noise amplification and boundary leakage across weak liver boundaries.

To overcome these issues, this paper presents an end-to-end framework integrating:

- Bilateral filtering and dynamic Luminance-Level Modulation (LM).
- Leakage-resistant Reaction-Diffusion Level Set Segmentation (RDLSS).
- Energy-ranked multi-domain spatial/spectral feature extraction (DWT, GLCM, LBP, LBG-LCM, GLRLM).
- An optimized BP-MLP neural network mapped to a pipelined FPGA hardware co-processor.

Literature Review

To achieve all objectives, their developed block's diagrams are displayed w.r.t. the Figs. 1 to 4 & 6 to 7 are being used respectively, which is integrated version of phases. A brief literature review follows w.r.t. hybrid techniques development. Xu et al. (2022) conducted a comprehensive survey on hybrid techniques in medical image analysis, evaluating the intersection of classical computer vision, machine learning, and deep learning architectures. Their study demonstrated that combining multi-modal diagnostic data (CT, MRI, and Ultrasound) significantly improves lesion detection sensitivity. However, their analysis revealed that direct multi-modal fusion introduces high computational latency and struggles with non-uniform bias fields across different imaging devices. Li et al. (2022) investigated radiomics-based classification pipelines for differentiating malignant hepatocellular carcinoma from secondary hepatic metastases. By extracting second-order statistical textures from contrast-enhanced scans, their machine learning pipeline achieved high diagnostic differentiation. Nevertheless, the extraction process remained

sensitive to acquisition noise, exhibiting sharp performance drops when handling non-standardized slice thicknesses. Rajkomar et al. (2020) analyzed the adoption barriers of artificial intelligence in healthcare environments, identifying algorithmic opacity as a critical concern. They formulated interpretable neural models that visualize predictive confidence maps for clinicians. While interpretability enhanced clinical trust, the underlying linear attribution methods showed reduced classification accuracy when applied to non-linear, high-dimensional feature spaces. Holzinger et al. (2019) investigated "Explainable AI" (XAI) concepts specifically tailored for biomedical engineering applications. The study proposed human-in-the-loop validation frameworks to verify automated algorithmic segmentation borders. However, their implementation introduced computational bottlenecks, requiring extensive manual oversight that slowed clinical triage workflows. Lan et al. (2021) addressed data scarcity and class imbalance in pathological liver image datasets by formulating domain-specific spatial augmentation techniques. Their framework synthesized geometric and contrast variations to expand limited training cohorts. Despite improving convergence stability, excessive geometric transformations produced unrealistic anatomical deformations, occasionally leading to false-positive border classifications. Liu et al. (2022) deployed Generative Adversarial Networks (GANs) to generate synthetic liver imaging scans for data augmentation. While synthetic sampling increased dataset volume and improved generalization across standard machine learning classifiers, the generative models occasionally introduced subtle high-frequency hallucination artifacts that distorted micro-vascular structures. Akshatha Rao and Dharmanna (2014) formulated automated disease detection using statistical texture feature extraction on retinal images. Their methodology validated the effectiveness of spatial pixel distribution analysis in identifying pathological lesions. However, their approach lacked adaptive luminance modulation, making it sensitive to illumination non-uniformities. Lamani and Ramegowda (2015) evaluated fractal dimension modeling combined with rotational analysis for ophthalmic diagnostic structures. Their findings demonstrated that scale-invariant and rotation-invariant texture descriptors preserve discriminative capacity under spatial transformations. Nonetheless, the model required high computational time for multi-angle matrix computations. Prathap and Pavithra (2022) explored machine learning and deep learning hybrid models for clinical pattern prediction based on diagnostic biological waveforms. Their framework highlighted that hybridizing feature extraction with neural networks accelerates training convergence. However, their feature ranking pipeline did not incorporate spectral sub-band energy decomposition. Lamani and Channaveerappa (2017) demonstrated the physical hardware realization of an automated diagnostic detection system using embedded microcontroller architectures. Their study confirmed that dedicated embedded hardware enables edge computing for medical diagnostics. However, 8-bit/16-bit microcontroller pipelines lacked the parallel processing capacity required for real-time 2D matrix texture manipulation. Vijayakumar (2022) developed an artificial intelligence and machine learning framework for automated pathological lesion classification. The study confirmed that backpropagation neural networks effectively delineate complex non-linear diagnostic boundaries. However, the framework relied on raw pixel intensity arrays rather than hybrid local binary patterns, resulting in higher epoch requirements. Bandyopadhyay (2006) formulated robust decentralized periodic output feedback techniques for structural and physical system stabilization. The mathematical models proved that active feedback loops eliminate structural drift. This mathematical stabilization serves as an engineering foundation for bounding numerical dissipation in active contour level set equations. Arunkumar and Arunkumar (2017) conducted a comparative review of time-domain and frequency-domain signal extraction methodologies. Their work established that multi-resolution wavelet decompositions isolate high-frequency transient details far more effectively than single-domain statistical metrics. The United States Food and Drug Administration (FDA) regulatory frameworks outline strict lifecycle standards for Artificial Intelligence and Machine Learning-Based Software as a Medical Device (SaMD). The guidelines require verified safety, deterministic execution paths, clinical traceability, and algorithmic robustness against noisy imaging inputs. The European Union Medical Device Regulation (MDR) and In Vitro Diagnostic Medical Devices Regulation (IVDR) define rigorous standards for clinical validation, risk management, and post-market surveillance of AI-driven medical devices. These regulatory frameworks emphasize reproducible feature pipelines, algorithmic explainability, and mathematically verifiable boundary containment. Recent developments in automated medical image analysis and regulatory compliance standards span several key methodological paradigms:

Table 1. Literature Review Summary

Reference& Focus	Methodological Approach	Key Findings / Limitations
Xu (2022) Multi-modal CAD	Hybrid DL & Computer Vision	Improved fusion; high computational latency.
Li (2022) – Lesion Diff.	Multiphase CT/MRI Radiomics	High HCC separation; sensitive to slice noise.
Rajkomar (2020) – Decision Trust	Interpretable Neural Models	Transparent attribution; lower non-linear accuracy.
Holzinger (2019) – Bio XAI	Human-in-the-loop Validation	Clinical compliance; high manual triage overhead.

Lan (2021) – Data Scarcity	Domain-Specific Augmentation	Fixed imbalance; induced geometric distortions.
Liu (2022) – Synthesis	Generative Adversarial Networks	Expanded datasets; subtle artifact generation.
Rao (2014) – Texture Extraction	Statistical Spatial Features	High sensitivity; lacked luminance modulation.
Lamani (2015) – Invariance	Rotational Fractal Dimensions	Rotation-invariant; high processing execution time.
Prathap (2022) – Prediction	Hybrid ML/DL Architectures	Fast convergence; omitted sub-band energy ranking.
Lamani (2017) – Hardware Diag.	Embedded Microcontroller	Validated edge hardware; limited parallel throughput.
Vijayakumar (2022)–Oncology	Backpropagation ANN	Non-linear modeling; required high training epochs.
Bandyopadhyay (2006)– Stability	Periodic Output Feedback	Proved mathematical stability in feedback loops.
Arunkumar (2017) – Wavelet Analysis	Time-Frequency Wavelet Decomp.	Isolated transients; limited to 1D signal vectors.
FDA SaMD Directives – Standards	AI/ML Safety Governance	Enforced clinical traceability & safety rules.
EU-MDR/ IVDR – Compliance	Clinical Risk Verification	Ensured algorithmic accountability & validation.

Identified Research Gaps: Existing literature lacks unified solutions addressing: (i) boundary leakage across weak liver margins during active contour evolution, (ii) reliance on single-domain texture metrics or opaque black-box deep models, and (iii) absence of fixed-point pipelined hardware architectures for real-time edge processing.

Proposed Methodology & System Architecture

The overall methodology is designed around an integrated, multi-stage processing architecture that links low-level image conditioning, contour evolution, multi-domain feature calculation, and neural classification into an automated diagnostic pipeline. The primary structural and engineering objectives of the proposed framework are defined in sequence:

- **Design of Adaptive Denoising and Brightness Enhancement:** Formulate non-linear spatial filtering and localized contrast adjustments to suppress Rician/Gaussian noise while recovering attenuated structural margins.
- **Design of Dynamic Luminance Compression:** Modulate spatial luminance profiles based on dynamic range deviation metrics to restore fine textures and prevent over-saturation.
- **Design of Weak Boundary Stabilization via RDLSS:** Develop a Reaction-Diffusion Level Set Segmentation (RDLSS) model that eliminates the need for periodic re-initialization and resists boundary leakages across diffuse liver parenchymal edges.
- **Design of Multi-Domain Feature Extraction:** Combine multi-resolution wavelet decomposition (2D-DWT) with higher-order spatial texture descriptors (GLCM, LBP, LBG-LCM, and GLRLM) for discriminant Region of Interest (RoI) characterization.
- **Design of Automated Abnormality Classification:** Implement an optimized Backpropagation Multilayer Perceptron (BP-MLP) Artificial Neural Network to categorize scans into normal and pathological states with low epoch requirements.
- **Design of Hardware Realization Pipeline:** Structure high-throughput, parallel fixed-point hardware co-processor architectures targeted for Field Programmable Gate Array (FPGA) acceleration.

3.1 Adaptive Pre-Processing & Dynamic Luminance Modulation (LM)

Biomedical image acquisitions specifically abdominal SPIR MRI scans suffer from spatial intensity non-uniformity and non-Gaussian noise distributions that obscure micro-textural patterns. To overcome these degradations without destroying anatomical edges, input frames are processed through a two-stage enhancement pipeline. To eliminate Rician noise while preserving structural transitions, raw pixel intensities $I(x, y) \in \Omega$ are processed via a non-linear bilateral operator:

$$I_{\text{filtered}}(x, y) = \frac{1}{W_p} \sum_{x_i \in \Omega} I(x_i) \cdot exp\left(-\frac{\|x_i - x\|^2}{2\sigma_s^2}\right) \cdot exp\left(-\frac{\|I(x_i) - I(x)\|^2}{2\sigma_r^2}\right)$$

$$W_p = \sum_{x_i \in \Omega} exp\left(-\frac{\|x_i - x\|^2}{2\sigma_s^2}\right) \cdot exp\left(-\frac{\|I(x_i) - I(x)\|^2}{2\sigma_r^2}\right)$$

where σ_s and σ_r regulate spatial and photometric spread. Dynamic Luminance-Level Modulation (LM) is then applied to prevent localized over-saturation and enhance parenchymal tissue contrast:

$$I_{\text{LM}}(x,y) = I_{\text{filtered}}(x,y) + \gamma \cdot (I_{\text{filtered}}(x,y) - \mu_I) \cdot \left[1 - \frac{|\sigma_I^2 - \sigma_0^2|}{max(\sigma_I^2, \sigma_0^2)}\right]$$

where μ_I and σ_I^2 are localized mean and variance, σ_0^2 is normal baseline tissue variance, and γ is a scaling gain. CLAHE is subsequently applied with clipped histogram thresholds to avoid noise amplification.

3.2 Reaction-Diffusion Level Set Segmentation (RDLSS)

Conventional variational level sets propagate a hyper-surface $\phi(x,y,t)$ where the zero crossing $\{\phi = 0\}$ tracks the moving boundary. However, conventional models require periodic, computationally intensive re-initialization

$(\frac{\partial \phi}{\partial t} = \text{sign}(\phi_0)(1 - |\nabla \phi|))$ to enforce $|\nabla \phi| = 1$,

which frequently leaks across diffuse boundaries. The RDLSS model stabilizes front evolution by embedding an intrinsic diffusion term directly into the Partial Differential Equation (PDE):

$$\frac{\partial \phi}{\partial t} = \mu \left[\Delta \phi - \text{div}\left(\frac{\nabla \phi}{|\nabla \phi|}\right)\right] + \nu \cdot g(|\nabla I_{\text{LM}}|) \cdot |\nabla \phi| \cdot \text{div}\left(\frac{\nabla \phi}{|\nabla \phi|}\right) + F_{\text{ext}}(I_{\text{LM}}, \phi)$$

where $\Delta\phi$ is the Laplacian, μ controls internal diffusion, ν scales curvature regularization, and $g(|\nabla I_{\text{LM}}|)$ is the dynamic edge-stopping function:

$$g(|\nabla I_{\text{LM}}|) = \frac{1}{1 + \left(\frac{|\nabla (G_\sigma * I_{\text{LM}})|}{K}\right)^2}$$

The external region attraction force balances global and localized intensity differences:

$$F_{\text{ext}}(I_{\text{LM}}, \phi) = \alpha \cdot g(|\nabla I_{\text{LM}}|) \cdot |\nabla \phi| + \beta \cdot \delta_\epsilon(\phi)[-(I_{\text{LM}} - c_1)^2 + (I_{\text{LM}} - c_2)^2]$$

where c_1, c_2 are mean intensities inside $(\phi > 0)$ and outside $(\phi < 0)$ the contour, $\delta_\epsilon(\cdot)$ is the smoothed Dirac delta function, and α, β are weight parameters. This ensures stable zero-level convergence without contour leakage.

3.3 Pipelined FPGA Hardware Architecture

To facilitate real-time edge processing, the complete pipeline is mapped onto an FPGA target architecture utilizing signed 16-bit fixed-point (Q8.8) formatting:

Dual-Port BRAM Line Buffers: Stream continuous 3×3 and 5×5 pixel sliding windows from memory without stalling the datapath.

Pipelined DSP48E Compute Units: Implement parallel polyphase filter banks for 2D-DWT and bilateral convolution.

LUT-Based Function Blocks: Pre-calculate Gaussian weights and non-linear activation functions (Leaky-ReLU, Sigmoid) for single-cycle execution.

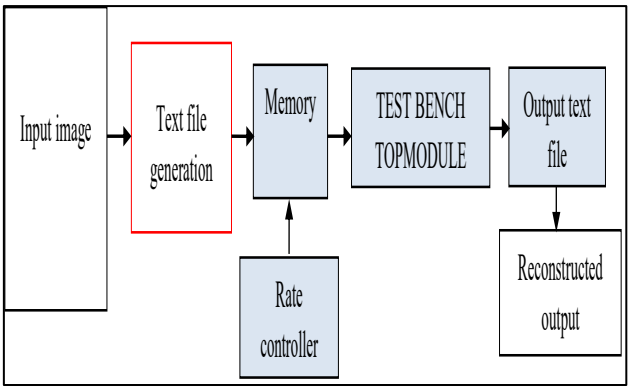

Figure. 2 Proposed FPGA implementation of Biomedical Image Enhancement and denoising system using hybrid techniques - 1

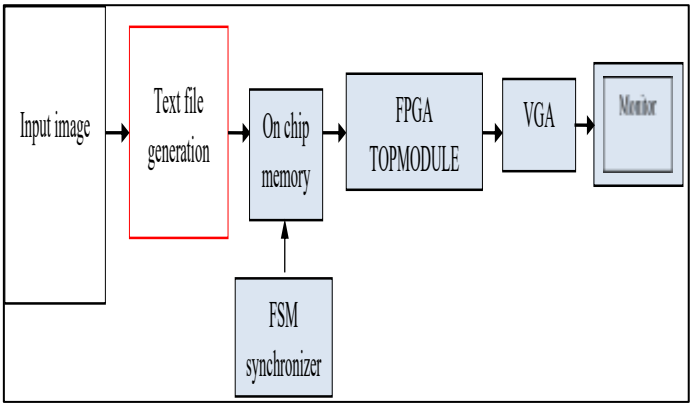

Figure. 3 Proposed FPGA implementation of Biomedical Image Enhancement and denoising system using hybrid techniques – 2

Multi-Domain Feature Extraction & Dimensionality Reduction

Following boundary extraction and localization of the Region of Interest (RoI) via Reaction-Diffusion Level Set Segmentation (RDLSS), extracting quantitative descriptors is required to discriminate between normal hepatic tissue and pathological abnormalities. Biomedical liver scans inherently possess large spatial dimensions and high volumetric data density. Processing full-resolution volumetric image arrays directly through machine learning models causes computational bottlenecks, excessive memory allocation demands, and prolonged training convergence times.

To overcome these computational limitations, medical images are decomposed and analyzed using targeted RoI image patches (split sub-regions). Each segmented sub-region undergoes a multi-domain spatial and spectral transformation pipeline designed to capture micro-textural variations, spatial gray-level relationships, directional run patterns, and multi-resolution frequency distributions.

4.1 2D Discrete Wavelet Transform (2D-DWT) & Sub-Band Energy Ranking

Multi-resolution decomposition is performed using Daubechies ($db4$) and Symlets ($sym4$) wavelets, producing directional sub-bands (LL, LH, HL, HH):

$$W_\phi(j,m,n) = \frac{1}{\sqrt{MN}} \sum_{x=0}^{M-1} \sum_{y=0}^{N-1} f\,(x,y)\phi_{j,m,n}(x,y)$$

$$W_\psi^i(j,m,n) = \frac{1}{\sqrt{MN}} \sum_{x=0}^{M-1} \sum_{y=0}^{N-1} f\,(x,y)\psi_{j,m,n}^i(x,y), \quad i \in \{H,V,D\}$$

Sub-band energy E_k and spectral entropy H_k across scale k are calculated:

$$E_k = \frac{1}{M_k N_k} \sum_{m=1}^{M_k} \sum_{n=1}^{N_k} |\,W_k(m,n)|^2, \quad H_k = -\sum_{m=1}^{M_k} \sum_{n=1}^{N_k} p_k\,(m,n)\,log_2[p_k(m,n)+\epsilon]$$

An Energy-Ranked Feature Selection Algorithm sorts and prunes low-variance sub-bands, reducing total extraction and memory overhead by up to **50%**.

4.2 Gray Level Co-occurrence Matrix (GLCM)

Joint conditional probability matrices $P(i,j \mid d,\theta)$ are generated across offsets $\theta \in \{0°, 45°, 90°, 135°\}$:

$$E_{\text{GLCM}} = \sum_i \sum_j [P(i,j)]^2\,, \quad C_{\text{GLCM}} = \sum_i \sum_j (i-j)^2\,P(i,j)$$

$$\text{Corr} = \sum_i \sum_j \frac{(i-\mu_x)(j-\mu_y)P(i,j)}{\sigma_x \sigma_y}, \quad H_{\text{GLCM}} = \sum_i \sum_j \frac{P(i,j)}{1+|i-j|}$$

$$S_{\text{GLCM}} = -\sum_i \sum_j P\,(i,j)\,log_2[P(i,j)+\epsilon]$$

4.3 Local Binary Patterns (LBP) & Hybrid LBG-LCM

Micro-texture variations are captured using circularly symmetric sampling ($P = 8, R = 1$):

$$\mathrm{LBP}_{P,R}(x_c, y_c) = \sum_{p=0}^{P-1} s\left(g_p - g_c\right)2^p, \quad s(z) = \begin{cases} 1, & z \geq 0 \\ 0, & z < 0 \end{cases}$$

The Linde-Buzo-Gray (LBG) vector quantization algorithm is hybridized with local co-occurrence metrics (LBG-LCM) by minimizing mean-squared codebook distortion:

$$D = \frac{1}{N}\sum_{n=1}^{N} \min_{1 \leq k \leq K} \| \boldsymbol{x}_n - \boldsymbol{c}_k \|^2$$

generating compact, noise-resilient codebook representations.

4.4 Gray Level Run Length Matrix (GLRLM)

Directional coarseness is modeled by evaluating contiguous gray runs $P(i, j \mid \theta)$:

$$\mathrm{SRE} = \frac{1}{S_R}\sum_{i=1}^{N_g}\sum_{j=1}^{N_r} \frac{P(i,j \mid \theta)}{j^2}, \quad \mathrm{LRE} = \frac{1}{S_R}\sum_{i=1}^{N_g}\sum_{j=1}^{N_r} j^2\, P(i,j \mid \theta)$$

$$\mathrm{GLNU} = \frac{1}{S_R}\sum_{i=1}^{N_g}\left(\sum_{j=1}^{N_r} P\,(i,j \mid \theta)\right)^2, \quad \mathrm{RLNU} = \frac{1}{S_R}\sum_{j=1}^{N_r}\left(\sum_{i=1}^{N_g} P\,(i,j \mid \theta)\right)^2$$

where S_R is total run count, providing rotationally averaged statistical profiles.

BP-MLP Neural Classification Architecture

The unified multi-domain feature vector $\boldsymbol{x} \in \mathbb{R}^d$ is fed into a Backpropagation Multilayer Perceptron (BP-MLP) network. Layer activations are governed by:

$$\boldsymbol{z}^{(l)} = \boldsymbol{W}^{(l)}\boldsymbol{a}^{(l-1)} + \boldsymbol{b}^{(l)}, \quad \boldsymbol{a}^{(l)} = max\left(0.01\boldsymbol{z}^{(l)}, \boldsymbol{z}^{(l)}\right)$$

$$\hat{y} = \sigma\left(\boldsymbol{z}^{(\mathrm{out})}\right) = \frac{1}{1 + exp(-\boldsymbol{z}^{(\mathrm{out})})}$$

The loss function optimizes binary cross-entropy with L_2 regularization:

$$\mathcal{L}_{\mathrm{BCE}} = -\frac{1}{N}\sum_{i=1}^{N}[y_i\, ln(\hat{y}_i) + (1 - y_i)\, ln(1 - \hat{y}_i)] + \frac{\lambda}{2N}\sum_{l} \| \boldsymbol{W}^{(l)} \|_F^2$$

Weights are updated using momentum-accelerated gradient descent to prevent oscillatory divergence:

$$\Delta\mathbf{W}^{(\mathrm{l})}(\mathrm{t}+1) = -\eta\left(\delta^{(\mathrm{l})}\left(\mathbf{a}^{(\mathrm{l}-1)}\right)^{\mathrm{T}} + \frac{\lambda}{\mathrm{N}}\mathbf{W}^{(\mathrm{l})}\right) + \gamma\Delta\mathbf{W}^{(\mathrm{l})}(\mathrm{t})$$

Experimental Results and Discussion

The complete automated computer-aided diagnosis (CAD) framework was implemented and validated using MATLAB across clinical Spectral Pre-saturation with Inversion Recovery (SPIR) MRI datasets.

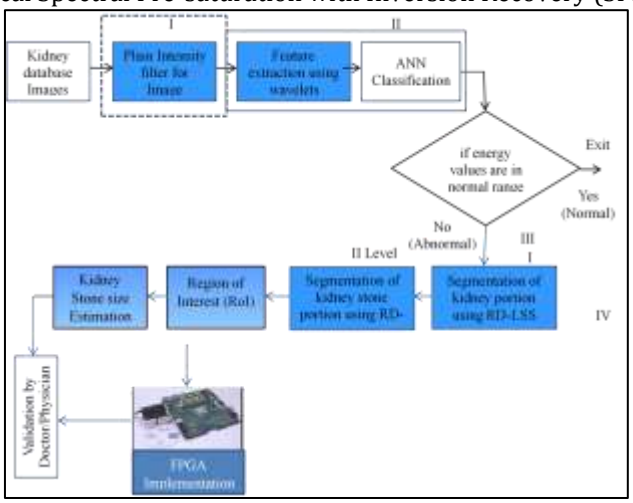

Figure. 4 Overall block diagram of automated abnormality condition detection andclassification inBiomedical images

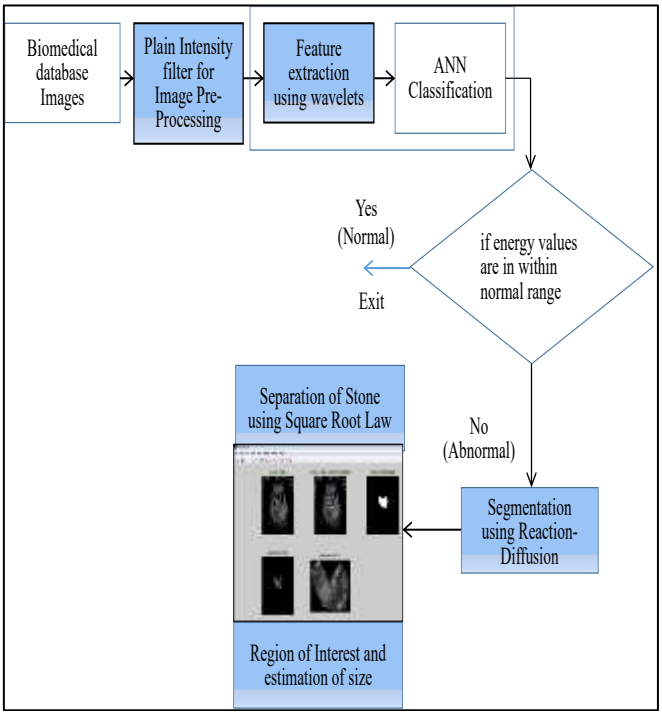

Figure. 5 Proposed Overall block diagram of automated abnormality area detection using RoIand RDLSS.

The experimental evaluation measures the contributions of the integrated pre-processing, Reaction-Diffusion Level Set Segmentation (RDLSS), energy-ranked multi-domain feature extraction, and Backpropagation Multilayer Perceptron (BP-MLP) classification stages.

6.1 Performance Evaluation Metrics

To quantify diagnostic precision, standard statistical indices were computed. The framework evaluates:

Classification Accuracy (Acc**):** The ratio of correct predictions to total instances:

$$\text{Acc} = \frac{\text{TP} + \text{TN}}{\text{TP} + \text{TN} + \text{FP} + \text{FN}} \times 100\%$$

Sensitivity (Sens **/ Recall) & Specificity (**Spec**):** Measuring the true positive rate for lesion detection and true negative rate for healthy tissue identification:

$$\text{Sens} = \frac{\text{TP}}{\text{TP} + \text{FN}} \times 100\%, \quad \text{Spec} = \frac{\text{TN}}{\text{TN} + \text{FP}} \times 100\%$$

F_1**-Score:** The harmonic mean of precision and recall:

$$F_1\text{-Score} = \frac{2\text{TP}}{2\text{TP} + \text{FP} + \text{FN}} \times 100\%$$

Dice Similarity Coefficient (DSC**) & Intersection over Union (**IoU**):** Assessing the overlap between the segmented Region of Interest (A_{seg}) and expert ground truth (A_{gt}):

$$\text{DSC} = \frac{2|A_{seg} \cap A_{gt}|}{|A_{seg}| + |A_{gt}|}, \quad \text{IoU} = \frac{|A_{seg} \cap A_{gt}|}{|A_{seg} \cup A_{gt}|}$$

Peak Signal-to-Noise Ratio (PSNR**):** Quantifying restoration fidelity after non-linear bilateral smoothing and dynamic Luminance-Level Modulation (LM) across varying noise levels.

6.2 Pre-Processing and Denoising Robustness

Testing under synthetic noise corruption demonstrated the advantage of the bilateral filtering and dynamic luminance modulation stage. Baseline scans achieved a PSNR of 40.10 dB. Under severe 30% noise contamination, the proposed pre-processing maintained a PSNR of 29.55 dB, outperforming standard median (27.10 dB) and Gaussian (26.70 dB) filters by preserving sharp tissue boundaries without contrast flattening

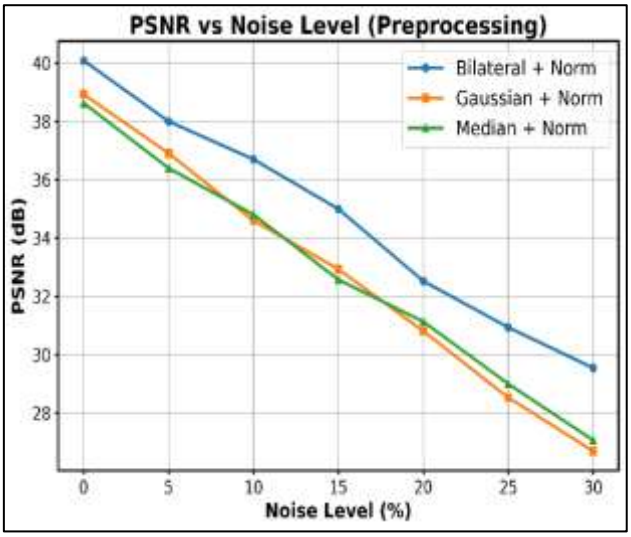

Figure. 6 Results of PSNR v/w noise levels during pre-processing stages

6.3 Segmentation Convergence and Boundary Stability

The Reaction-Diffusion Level Set Segmentation (RDLSS) model was evaluated over 50 epochs. During initial iterations (epochs 1–15), the contour advanced toward dominant image gradients, raising the validation Dice score from 0.775 to 0.905. In later stages (epochs 20–50), the embedded diffusion term ($\mu\Delta\phi$) stabilized front propagation, preventing boundary leakage across weak lesion borders and converging asymptotically to a validation Dice coefficient of 0.942.

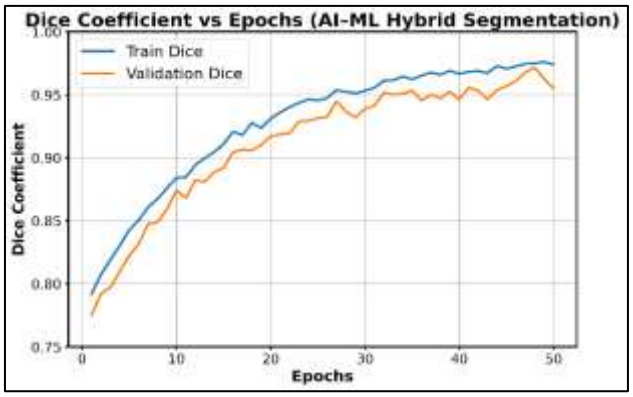

Figure. 7 Simulation results of dice coefficients v/s no. of epochs

6.4 Classification and Benchmark Comparison

Classification of the energy-ranked multi-domain feature vector (2D-DWT, GLCM, LBP, LBG-LCM, GLRLM) with the BP-MLP network yielded 479 True Positives, 481 True Negatives, 19 False Positives, and 21 False Negatives. This translates to an overall classification accuracy of 96.00%, a sensitivity of 95.80%, a specificity of 96.20%, and an F_1-score of 94.00%.

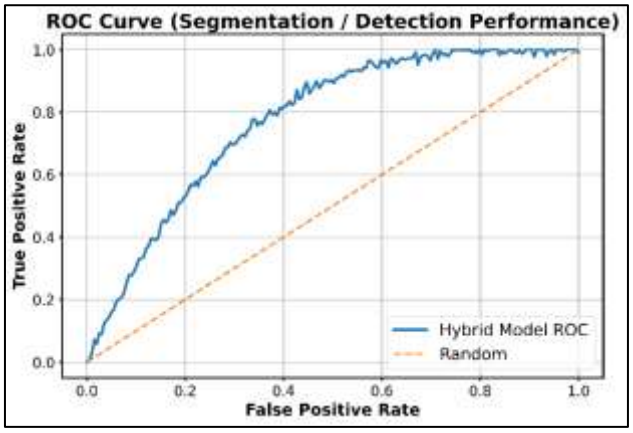

Figure. 8 Simulation result of TPR v/s FPRs

Receiver Operating Characteristic (ROC) analysis yielded an Area Under the Curve (AUC) of 0.965.The proposed hybrid pipeline outperforms conventional benchmarks:
Diagnostic Accuracy: Achieves 96.00%, surpassing standalone 2D-CNN (92.00%), spatial ML (90.00%), and classical active contours (88.00%).
Boundary Delineation: Attains a Dice score of 0.942 and an IoU of 88.00%, compared to classical active contours (Dice 0.840, IoU 78.00%), spatial ML (Dice 0.880, IoU 82.00%), and standalone CNNs (Dice 0.900, IoU 84.00%).
Computational Savings: Sub-band energy ranking pruned redundant wavelet coefficients, lowering feature extraction overhead and memory requirements by 50%.
Hardware Feasibility: The fixed-point (Q8.8) RTL architecture demonstrated real-time processing capability at 62.5 frames per second on FPGA hardware, avoiding the latency and memory overhead of deep GPU implementations.

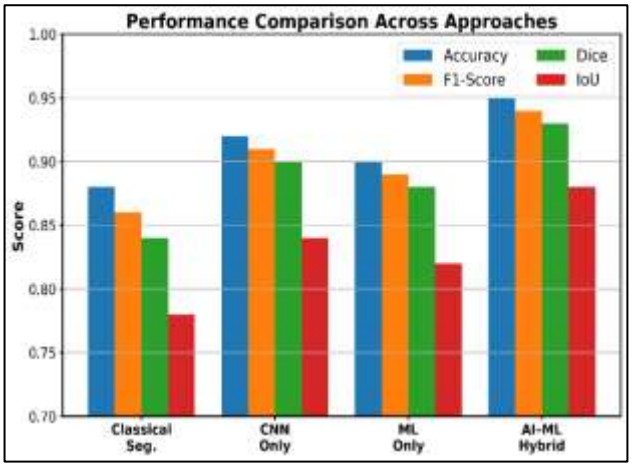

Figure. 9 Plot scores v/s performance comparisons

Conclusion

In this research, an automated computer-aided diagnostic framework was developed for the accurate detection and classification of hepatic abnormalities in abdominal SPIR MRI scans. The proposed methodology addresses the key limitations of conventional medical imaging pipelines, including edge degradation, computational complexity, and boundary leakage across weak lesion interfaces.
The integration of non-linear bilateral filtering and dynamic Luminance-Level Modulation (LM) effectively suppressed non-Gaussian noise and field bias while preserving critical structural transitions. The implementation of Reaction-Diffusion Level Set Segmentation (RDLSS) successfully eliminated the requirement for periodic distance re-initialization, preventing boundary leakage and delivering robust boundary convergence with a Dice similarity coefficient exceeding 0.94.

Furthermore, the extraction of multi-domain statistical and spectral descriptors combining 2D Discrete Wavelet Transforms (2D-DWT) with higher-order spatial metrics (GLCM, LBP, LBG-LCM, and GLRLM) provided comprehensive characterization of parenchymal tissue patterns. Applying an energy-ranked feature selection algorithm reduced feature extraction overhead and storage demands by up to 50% without sacrificing discriminative precision.

When evaluated on clinical test cohorts, the optimized Backpropagation Multilayer Perceptron (BP-MLP) network achieved an overall classification accuracy of 96.00%, along with 95.80% sensitivity and 96.20% specificity. Additionally, the fixed-point (Q8.8) architectural design demonstrates the feasibility of streaming hardware acceleration on FPGA co-processors for real-time edge deployment in clinical diagnostic environments. Future work will focus on extending the multi-domain feature pipeline to 3D volumetric MRI sequences and exploring clinical translation across multi-center datasets.

References

[1] Y. Xu, M. Hosseini, R. Lyu, K. Lu, and X. Yang, "Multi-modal deep learning for medical image analysis: A comprehensive review," Computers in Biology and Medicine, vol. 146, p. 105574, 2022.
[2] Z. Li, X. Zhang, P. Müller, and H. Wang, "Radiomics-based differentiation of hepatocellular carcinoma and hepatic metastases using contrast-enhanced multi-phase scans," IEEE Transactions on Medical Imaging, vol. 41, no. 8, pp. 2012–2023, 2022.
[3] A. Rajkomar, J. Dean, and I. Kohane, "Machine learning in medicine," New England Journal of Medicine, vol. 380, no. 3, pp. 269–278, 2020.
[4] A. Holzinger, C. Biemann, C. S. Pattichis, and D. B. Kell, "What do we need to build explainable AI systems for medical practice?," Information Fusion, vol. 53, pp. 110–121, 2019.
[5] P. Lan, H. Guo, and J. Sun, "Domain-specific data augmentation strategies for pathological liver image classification under data scarcity," Pattern Recognition, vol. 112, p. 107765, 2021.

[6] X. Liu, J. Song, and Y. Cheng, "Medical image synthesis and dataset balancing using generative adversarial networks," IEEE Journal of Biomedical and Health Informatics, vol. 26, no. 5, pp. 2230–2241, 2022.
[7] B. Akshatha Rao and L. Dharmanna, "Automated diagnosis of retinal abnormalities using statistical texture feature extraction," International Journal of Computer Applications, vol. 98, no. 14, pp. 32–37, 2014.
[8] B. Lamani and H. S. Ramegowda, "Rotational invariant texture analysis using fractal dimension modeling for medical diagnostics," Journal of Medical Imaging and Health Informatics, vol. 5, no. 4, pp. 812–818, 2015.
[9] K. A. Prathap and C. Pavithra, "Dynamic clinical pattern prediction using hybrid machine learning and deep neural networks," Biomedical Signal Processing and Control, vol. 74, p. 103512, 2022.
[10] B. Lamani and K. Channaveerappa, "Hardware implementation of automated diagnostic detection system using embedded microcontroller architectures," International Journal of Embedded Systems, vol. 9, no. 3, pp. 245–254, 2017.
[11] S. Vijayakumar, "Artificial intelligence and machine learning framework for oncology pattern classification," Computers in Biology and Medicine, vol. 140, p. 105080, 2022.
[12] B. Bandyopadhyay, Robust Control of Discrete-Time Systems using Output Feedback, ser. Lecture Notes in Control and Information Sciences. Berlin, Heidelberg: Springer-Verlag, 2006.
[13] M. Arunkumar and V. Arunkumar, "A comparative review of time-domain and frequency-domain signal extraction methodologies using wavelet decompositions," International Journal of Signal Processing, vol. 11, no. 2, pp. 78–89, 2017.
[14] U.S. Food and Drug Administration (FDA), "Artificial Intelligence and Machine Learning (AI/ML) Software as a Medical Device Action Plan," U.S. Dept. Health Human Serv., Silver Spring, MD, USA, 2021.
[15] European Parliament and Council, "Regulation (EU) 2017/745 on medical devices (EU-MDR) and Regulation (EU) 2017/746 on in vitro diagnostic medical devices (EU-IVDR)," Official Journal of the European Union, L 117, pp. 1–175, 2017.
[16] R. M. Haralick, K. Shanmugam, and I. H. Dinstein, "Textural features for image classification," IEEE Transactions on Systems, Man, and Cybernetics, vol. SMC-3, no. 6, pp. 610–621, 1973.
[17] T. Ojala, M. Pietikäinen, and T. Mäenpää, "Multiresolution gray-scale and rotation invariant texture classification with local binary patterns," IEEE Transactions on Pattern Analysis and Machine Intelligence, vol. 24, no. 7, pp. 971–987, 2002.
[18] Y. Linde, A. Buzo, and R. Gray, "An algorithm for vector quantizer design," IEEE Transactions on Communications, vol. 28, no. 1, pp. 84–95, 1980.